Liquid-liquid phase separation of PHLDB2 promotes oral squamous cell carcinoma metastasis through regulating epithelial mesenchymal transition and PIK3CA expression

KUNYI CHEN[1-3*], YUHONG WANG[1-3*], JIANING CUI[1-3], QIANRUI LIU[1-3], XIAOYONG LIU[1-3], WENJIN WANG[1-3] and JINSONG HOU[1-3]

[1]Department of Oral and Maxillofacial Surgery, Hospital of Stomatology, Sun Yat-sen University, Guangzhou, Guangdong 510055, P.R. China; [2]Guanghua School of Stomatology, Sun Yat-sen University, Guangzhou, Guangdong 510055, P.R. China; [3]Guangdong Provincial Key Laboratory of Stomatology, Sun Yat-sen University, Guangzhou, Guangdong 510080, P.R. China

Received April 28, 2025; Accepted July 24, 2025

DOI: 10.3892/mmr.2025.13720

Abstract. Liquid-liquid phase separation (LLPS) contributes to multiple cellular bioprocesses; however, its clinicopathological relevance to oral squamous cell carcinoma (OSCC) remains largely unexplored. In the present study an integrative multi-omics analysis investigating the prognostic value and molecular functions of LLPS-related genes (LLPSRGs) in OSCC was conducted by leveraging transcriptomics and clinical data from 302 cases in The Cancer Genome Atlas database and LLPSRGs. A total of two prognostically distinct molecular subtypes were stratified by unsupervised clustering analysis, and a robust prognostic signature comprising seven key LLPSRGs was developed through LASSO regression and multivariate Cox analysis. Functional enrichment analysis highlighted the involvement of this signature in epithelial-mesenchymal transition (EMT), with PHLDB2 emerging as a core regulator. Notably, the PHLDB2 protein underwent LLPS and formed droplet condensates both outside and in OSCC cells. Moreover, functional experiments revealed that PHLDB2 depletion attenuated the malignant biological behavior of OSCC cells, including cell proliferation, stemness, invasion and migration, and PHLDB2 promoted OSCC progression by regulating the PI3K-Akt signaling pathway and PIK3CA expression. Retrospective clinical cohort and public dataset analyses validated that high expression of PHLDB2 was significantly associated with lymph node metastasis, higher pathological grade and reduced survival in patients with OSCC. Collectively, the present study established an LLPS-based prognostic signature for OSCC, and revealed that phase separation of PHLDB2 may drive OSCC progression through regulating EMT and PIK3CA.

Correspondence to: Professor Jinsong Hou or Dr Wenjin Wang, Department of Oral and Maxillofacial Surgery, Hospital of Stomatology, Sun Yat-sen University, 56 Lingyuan Road West, Guangzhou, Guangdong 510055, P.R. China
E-mail: houjs@mail.sysu.edu.cn
E-mail: wangwj96@mail2.sysu.edu.cn

*Contributed equally

Key words: liquid-liquid phase separation, oral squamous cell carcinoma, PHLDB2

Introduction

Oral squamous cell carcinoma (OSCC) is the most common malignant tumor in the maxillofacial region; globally, there are 380,000 new cases of OSCC diagnosed and 180,000 OSCC-associated deaths recorded in 2022 (1). Although surgery, radiotherapy and chemotherapy have shown efficacy in early-stage OSCC, the high invasiveness and metastatic tendency of OSCC often lead to local recurrence and distant dissemination (2). Therefore, identifying the molecular mechanisms underlying the malignant progression of OSCC and developing novel therapeutic strategies is required.

Recently, liquid-liquid phase separation (LLPS) has emerged as a fundamental paradigm for regulating cellular functions. Through weak interactions between intrinsically disordered regions (IDRs), multivalent proteins or nucleic acid scaffolds, biomacromolecules dynamically undergo LLPS to form membraneless organelles, and precisely regulate key biological processes such as transcription, epigenetic modification and signal transduction (3,4). Accumulating evidence has suggested that abnormal LLPS contributes to various oncogenic processes, including the evasion of tumor cell senescence, stemness maintenance and metastatic spread (5,6). For example, cancer cells can evade senescence and death by activating telomerase or via alternative lengthening of telomeres (ALT) (7). After telomeric DNA damage in cancer stem cells, ALT-associated proteins undergo LLPS through interactions between small ubiquitin-like modifiers (SUMOs) and SUMO-interacting motifs, forming ALT-associated promyelocytic leukemia bodies that mediate telomere repair (8). Additionally, Lu *et al* (9) reported that the transcriptional coactivator TAZ forms nuclear condensates through IDR-mediated LLPS, colocalizing with transcriptional complexes such as

TEAD4 and BRD4. Notably, the loss of the phase separation ability of TAZ can inhibit target gene expression and tumor metastasis. Beyond transcriptional regulation, LLPS also serves an important role in post-transcriptional modification. In acute myeloid leukemia, the m6A reader protein YTHDC1 interacts with m6A-modified mRNA through LLPS to form nuclear condensates, regulating RNA splicing and transport (10). Furthermore, LLPS has reshaped the understanding of signal transduction mechanisms. Tulpule *et al* (11) demonstrated that receptor tyrosine kinases can form membraneless protein granules through LLPS, enriching the GRB2/SOS1 complex and activating the RAS/MAPK pathway, challenging the traditional lipid membrane-dependent signal transduction model.

Notably, LLPS drives biomolecular condensation in cancer progression, with LLPS-related genes (LLPSRGs) establishing prognostic value in ovarian (12), breast (13) and bladder cancer (14). However, OSCC, a tumor shaped by unique etiological factors (use of tobacco and alcohol, human papillomavirus infection) and frequent recurrence, lacks systematic investigation into LLPS dysregulation. The following critical gaps in the knowledge persist: i) No specific research has been conducted to clarify the prognostic value of LLPSRGs in OSCC; ii) mechanistic links between LLPSRG-mediated dysregulation and aggressive OSCC phenotypes are undefined. These gaps hinder therapeutic targeting of LLPS vulnerabilities in this molecularly complex carcinoma.

The present study aimed to establish the first dedicated investigation of LLPS in OSCC, with the following objectives: i) To identify OSCC-specific LLPSRGs through multi-omics integration; and ii) to elucidate the mechanistic role of biomolecular condensates in driving OSCC invasion. Ultimately, by connecting LLPS dynamics to the molecular landscape of OSCC, the current study intended to discover novel phase separation-derived biomarkers and therapeutic targets for precision oncology.

Materials and methods

Acquisition of public datasets. LLPSRGs (n=3,633) were retrieved from the Data Resource of LLPS (DrLLPS; https://llps.biocuckoo.cn/). Transcriptomics profiles and clinical records from an OSCC cohort (n=302), whose primary lesion sites were the tongue, base of the tongue, buccal mucosa, oral cavity, floor of the mouth and gingiva, were obtained from The Cancer Genome Atlas (TCGA; https://www.cancer.gov/ccg/research/genome-sequencing/tcga). The GSE213862 dataset from the Gene Expression Omnibus (GEO; http://www.ncbi.nlm.nih.gov/geo/) was also acquired, comprising transcriptomics data from 47 pairs of OSCC tissues and normal mucosal tissues (15).

Identification of two distinct LLPS-associated molecular clusters. Consensus clustering analysis was conducted using the R package 'ConsensusClusterPlus' (16) to stratify TCGA-OSCC samples into distinct molecular clusters (C1 and C2) based on the expression profiles of LLPSRGs. Cluster stability was evaluated by analyzing the cumulative distribution function (CDF) of the consensus matrix across multiple k-values. Differentially expressed genes (DEGs) between C1 and C2 were identified using the R package 'DESeq2' (17), based on the criteria of |log2 fold change (FC)|>1 and P<0.05. Survival analysis between C1 and C2 were conducted using the R package 'survival' (https://github.com/therneau/survival).

Construction of a prognostic prediction model based on LLPSRGs for OSCC. TCGA-OSCC cohort was randomly divided into training and validation subsets at a ratio of 7:3. Univariate Cox regression and LASSO regression analyses (implemented via the R packages 'survival' and 'glmnet' (https://glmnet.stanford.edu) were applied to the training cohort to screen seven LLPSRGs significantly associated with OSCC prognosis. A risk score model was established using LASSO-derived coefficients, and patients in both the training and validation cohorts were stratified into high- or low-risk groups based on the median risk score. Model performance was evaluated through Kaplan-Meier curve analysis with Wilcoxon test, time-dependent receiver operating characteristic (ROC) curves, principal component analysis (PCA) and t-distributed stochastic neighbor embedding (t-SNE) using 'survival', 'timeROC' (https://github.com/cran/timeROC), 'Rtsne' (https://github.com/jkrijthe/Rtsne) and the related visualization tool 'ggplot2' (https://github.com/tidyverse/ggplot2). The prognostic nomogram was constructed by integrating the continuous risk score with established clinical variables: Tumor-Node-Metastasis (TNM) stage, histological grade and age, using R package 'rms' (https://github.com/harrelfe/rms).

Differential expression analysis and gene set enrichment analysis (GSEA). Differential expression analysis between the high- and low-risk groups was conducted using the R package 'DESeq2' (16) and 'limma' (https://bioinf.wehi.edu.au/limma), based on the criteria of P<0.05 and |log2FC|>1. The Minus-vs.-Add (MA) plot visualizing differential expression patterns between risk groups was generated using the R package 'limma'. Gene Ontology (GO), Kyoto Encyclopedia of Genes and Genomes (KEGG) enrichment analyses and Hallmark GSEA based on the Molecular Signatures Database (MsigDB; https://www.gsea-msigdb.org/gsea/msigdb) of DEGs was conducted using R packages 'enrichplot' (https://github.com/YuLab-SMU/enrichplot)and'clusterProfiler'(https://github.com/YuLab-SMU/clusterProfiler).

Public single-cell RNA sequencing (scRNA-seq) data collection and analysis. The scRNA-seq data analyzed in the present study were accessible via the GEO accession number, GSE234933 (18). Based on clinical metadata from GSE234933, samples were categorized into the primary lesion (sample count, 19; cell count, 123,094) and metastatic lesion (sample count, 8; cell count, 38,987) groups. The R package 'Seurat' (https://github.com/satijalab/seurat; version 4.3.0) was used for initial quality control removing cells with <200 detected genes. Validated cell data were integrated into a Seurat object for downstream analysis. Distinctly expressed genes were detected with single-cell resolution using the FindAllMarkers tool implemented in Seurat.

LLPS potential evaluation for model genes. The GEPIA2 website (http://gepia2.cancer-pku.cn/) (19) was used to compare the relative expression of model genes in TCGA-OSCC.

The IDRs of model genes were identified using IUPred2, while their disordered binding regions were characterized via ANCHOR2 analysis through the IUPred2A platform (https://iupred2a.elte.hu/) (20). LLPS propensity scoring of the model genes was performed using PhaSePred (http://predict.phasep.pro/) (21), incorporating the following computational algorithms: catGRANULE, PdPS-10fea, SaPS-10fea, PdPS-8fea, SaPS-8fea, DeepPhase, Phos, Charged residue, SEG, Hydropathy, ESpritz-DisProt, PScore and PLAAC.

In vitro droplet formation assay. PHLDB2 protein solutions (cat. no. Ag27331; Proteintech Group, Inc.) was conjugated with Alexa Fluor 488 (cat. no. ab236553; Abcam). Fluorescently labeled recombinant PHLDB2 protein was purified and reconstituted in NaCl solutions at physiologically relevant concentration gradients, ranging from 50 to 500 mM. Subsequently, the preparations were immediately combined with a phase separation buffer containing 10% glycerol, 50 mM Tris-HCl (pH 7.4), 1 mM DTT and 10% PEG-8000, serving as a molecular crowding agent. After incubation at room temperature for 5 min, the mixture was pipetted onto glass slides prepared with coverslips secured by double-sided adhesive spacers. Imaging was performed using a confocal microscope (LSM980; Zeiss AG) equipped with a 63X objective lens.

Cell lines and culture conditions. The present study employed two human OSCC lines: SCC1 and HSC3, obtained from the University of Michigan (Ann Arbor, MI, USA). HSC3 cells were cultured in DMEM (cat. no. C11995500BT; Gibco; Thermo Fisher Scientific, Inc.) and SCC1 cells were cultured in DMEM/F-12 medium (cat. no. C11330500BT; Gibco; Thermo Fisher Scientific, Inc.). Both media were supplemented with 10% FBS (cat. no. 10099-141C; Gibco; Thermo Fisher Scientific, Inc.) and 1% penicillin-streptomycin (cat. no. 15140122; Gibco; Thermo Fisher Scientific, Inc.). Cells were maintained at 37˚C in a humidified incubator containing 5% CO_2.

Transient small interfering RNA (siRNA) and PHLDB2-EGFP plasmid transfection. The oligonucleotide sequences for siRNA and the PHLDB2-EGFP plasmid are provided in Table SI. SCC1 and HSC3 OSCC cells at 60-80% confluence were transfected with PHLDB2-targeting siRNAs or control siRNAs (50 nM) and the PHLDB2-EGFP plasmid (1 μg/ml) using Lipofectamine® RNAiMAX (cat. no. 13778150; Invitrogen; Thermo Fisher Scientific, Inc.) according to the manufacturer's protocol. Transfection was performed at 37˚C for 48 h and subsequent experiments were conducted 24 h post-transfection.

Fluorescence recovery after photobleaching (FRAP) analysis. FRAP analysis was performed using an LSM980 confocal microscope (Zeiss AG). SCC1 cells expressing EGFP-tagged PHLDB2 were visualized with a 63X oil-immersion objective. Phase-separated condensates were selectively bleached using a 488-nm laser at 98% intensity. Post-bleaching recovery was tracked by capturing sequential images at 1-sec intervals for 100 sec. Droplet fluorescence intensities were analyzed using ZEN Microscopy Software (version 3.0; Carl Zeiss AG), and recovery kinetics were plotted with GraphPad Prism 9.0 (Dotmatics).

Reverse transcription-quantitative PCR (RT-qPCR). Total RNA isolation was carried out using TRIzol® reagent (cat. no. 15596018; Invitrogen; Thermo Fisher Scientific, Inc.), followed by cDNA synthesis using the PrimeScript RT Reagent Kit (cat. no. RR047A; Takara Bio, Inc.) according to the manufacturer's protocol. qPCR was conducted on a Roche LightCycler 96 platform (Roche Diagnostics) employing SYBR Green PCR Master Mix (cat. no. 11201ES08; Shanghai Yeasen Biotechnology, Co., Ltd.). The qPCR amplification protocol consisted of an initial denaturation step at 95˚C for 5 min, followed by 40 cycles of denaturation at 95˚C for 10 sec, annealing at 60˚C for 20 sec and extension at 72˚C for 20 sec. GAPDH was used as the reference gene for normalization. Relative gene expression was calculated using the $2^{-\Delta\Delta Cq}$ method (22). Primer sequences, designed against GenBank (https://www.ncbi.nlm.nih.gov/genbank) reference data, are compiled in Table SII.

Western blotting. Protein extraction was performed with ice-cold RIPA lysis buffer (cat. no. CW2333S; Jiangsu CoWin Biotech Co., Ltd.) containing protease inhibitor cocktail. Protein concentrations were determined using a BCA quantification kit (cat. no. CW0014S; Jiangsu CoWin Biotech Co., Ltd.) according to standardized protocols. The lysates (control-si 5.26 mg/ml; PHLDB2si-1 4.94 mg/ml; PHLDB2si-2 5.04 mg/ml) were electrophoretically separated by SDS-PAGE on 10% gels, followed by semi-dry transfer to PVDF membranes (cat. no. ISEQ00010; MilliporeSigma). The membranes were then subjected to blocking with 5% milk in TBS with 0.05% Tween at room temperature for 1 h, and incubated with primary antibodies at 4˚C for 16 h. After washing and incubation with HRP-conjugated secondary antibodies at 25˚C for 1 h, immunoreactive bands were detected using ECL substrate (cat. no. WBKLS0500; MilliporeSigma) and semi-quantified with a GeneGnome XRQ imaging system (Syngene; software version, GeneSys 2023). The following primary antibodies were used: Rabbit polyclonal anti-PHLDB2 (cat. no. ab234885; 1:1,000; Abcam), E-cadherin (cat. no. ab231303; 1:2,000; Abcam), N-cadherin (cat. no. ab76011; 1:5,000; Abcam), vimentin (cat. no. ab92547; 1:1,000; Abcam) and mouse monoclonal anti-GAPDH (cat. no. ab8245; 1:5,000; Abcam). The following secondary antibodies were used: Goat Anti-Rabbit IgG H&L (HRP) (cat. no. ab205718; 1:10,000; Abcam) and Goat Anti-Mouse IgG H&L (HRP) (cat. no. ab205719; 1:10,000; Abcam).

Cell Counting Kit-8 (CCK-8) cell proliferation assay and colony formation assay. Cell proliferation was assessed using the CCK-8 assay. HSC3 and SCC1 cells ($2x10^3$ cells/well) were plated and treated with 10% CCK-8 reagent (Sigma-Aldrich; Merck KGaA) in DMEM. Absorbance was measured after a 2 h-incubation to determine cell viability. For colony formation analysis, after 1 week of culturing cells seeded at an initial density of 1,000 cells per well in 6-well plates, colonies were fixed with 4% paraformaldehyde for 20 min and stained with 0.5% crystal violet (cat. no. C3886; Sigma-Aldrich; Merck KGaA) for 20 min at room temperature, and images were

then captured. Colonies defined as cell aggregates containing ≥50 cells within a 0.3-1.0 mm diameter were quantified using ImageJ software (version 1.54p; National Institutes of Health).

Spheroid formation assay and limiting dilution assay. Cells were plated in ultra-low attachment 96-well plates at graded densities ($1x10^3$, $5x10^2$, $2x10^2$, $1x10^2$ and $5x10^1$ per well) using serum-free DMEM/F-12 containing 2% B27 (cat. no. 17504044; Gibco; Thermo Fisher Scientific, Inc.), 20 ng/ml hEGF (cat. no. 105-04; PrimeGene) and 10 ng/ml hFGF (cat. no. 104-02; PrimeGene). Cultures were maintained under 5% CO_2 at 37˚C with quintuplicate wells/density. After a 10-day incubation, images of spheroids were captured using an inverted light microscope (Zeiss Axio Observer; Carl Zeiss AG), and quantified using ImageJ software (version 1.54p; National Institutes of Health). Cancer stem cell frequency was determined using ELDA computational analysis (http://bioinf.wehi.edu.au/software/elda/).

Wound healing assay and invasion assay. For wound healing evaluation, OSCC cells were cultured to 90% confluence in 6-well plates, and a linear wound was introduced to monolayers using a 200-μl pipette tip. Migration progression was documented at 0, 12, 16 and 24 h intervals through phase-contrast light microscope (Zeiss Axio Observer; Carl Zeiss AG), with wound closure quantified using ImageJ software (version 1.54p; National Institutes of Health). For Transwell invasion assays, the upper chambers were precoated with Matrigel (cat. no. 354234; Corning, Inc.) at 4˚C and incubated at 37˚C for 30 min. Subsequently, $2x10^4$ cells/well were loaded into Matrigel-precoated upper chambers (cat. no. 354234; Corning, Inc.) in serum-free medium. The lower chambers contained 10% FBS as a chemoattractant. After a 48-h incubation at 37˚C, cells on the membrane were fixed with 4% paraformaldehyde at room temperature for 20 min and stained with 0.1% crystal violet for 20 min at room temperature. Invasive cells were counted under bright-field microscopy.

RNA-seq. RNA was extracted from SCC1 cells, with RNA purity quantified by Nanodrop (Thermo Fisher Scientific, Inc.) and integrity assessed using an Agilent 4200 TapeStation (Agilent Technologies, Inc.). Libraries were constructed from 1 μg RNA using the TruSeq Stranded mRNA Library Prep Kit (cat. no. 20020594; Illumina, Inc.) according to the manufacturer's protocol. Briefly, mRNA underwent fragmentation using divalent cations, followed by first-strand cDNA synthesis with reverse transcriptase and second-strand synthesis using DNA polymerase I/dNTPs. Double-stranded cDNA was processed through end repair, A-tailing and adapter ligation (200-300 bp size selection). Libraries were size-selected (200-300 bp) using AMPure XP beads. After 12 cycles of PCR amplification, final libraries were purified and quality-controlled using an Agilent 2100 Bioanalyzer High Sensitivity DNA Assay (cat. no. 5067-4626; Agilent Technologies, Inc.). The loading concentration of the final library was 14 nM for control-si group and 15 nM for PHLDB2-si group. Quality-controlled libraries were pooled and diluted to 1.8 nM in 10 mM Tris-HCl (pH 8.5) based on Qubit dsDNA HS Assay measurements (cat. no. Q32854; Thermo Fisher Scientific, Inc.). Paired-end sequencing (2x150 bp) was performed on an Illumina NovaSeq 6000 system using the NovaSeq 6000 SP Reagent Kit v1.5 (100 cycles; cat. no. 20027464) (both from Illumina, Inc.). Bioinformatics analysis identified DEGs between the control group and the PHLDB2-knockdown group using DESeq2 ($|log2FC|>1$; $P<0.05$), followed by functional enrichment analysis to characterize biological pathways using the R package 'clusterProfiler' (https://github.com/YuLab-SMU/clusterProfiler). Core PI3K-Akt signaling components were retrieved from the KEGG PI3K-Akt signaling pathway gene set. Differential expression of these components between control and PHLDB2 knockdown groups was analyzed with the R package 'limma', followed by visualization as a heatmap using the R package 'ggplot2'.

Patients and specimens. The Sun Yat-sen University (SYSU)-OSCC cohort retrospectively analyzed clinicopathological data from 51 treatment-naïve patients treated between June 2016 and June 2018. The cohort comprised 35 men and 16 women, with a mean age of 52 years (range: 26-77 years). These data were used for validation in the present study. All participants underwent surgical resection of primary tumors with cervical lymph node dissection at the Hospital of Stomatology, SYSU (Guangzhou, China) with no presurgical adjuvant therapy. Clinicopathological parameters and survival data were retrieved through clinical documentation and structured telephone follow-ups. Tumor staging followed the Union for International Cancer Control 8th edition TNM guidelines (23). The present study received approval from the ethics committee of the Hospital of Stomatology, SYSU (approval no. KQEC202013) and all participants provided written informed consent.

Immunohistochemical (IHC) staining. IHC staining was performed on 4-μm-thick paraffin-embedded tissue sections. Sections were blocked with 10% goat serum (cat. no. SL038; Beijing Solarbio Science & Technology Co., Ltd.) in PBS for 30 min at room temperature. Primary antibodies were diluted as follows: Anti-PHLDB2 (1:50; cat. no. ab234885; Abcam) and IgG isotype control antibody (1:100; cat. no. ab172730; Abcam), and incubated overnight at 4˚C. Following primary antibody incubation, sections were incubated with the appropriate secondary antibody (1:100 dilution) for 30 min at room temperature. IHC staining was then conducted with anti-rabbit/mouse HRP/DAB (ABC) detection kits (cat. nos. ab64261 and ab64259; Abcam) according to the manufacturer's protocol. Secondary antibodies were diluted as follows: Goat Anti-Rabbit IgG H&L (1:5,000; cat. no. ab205718; Abcam) and Goat Anti-Mouse IgG H&L (1:5,000; cat. no. ab205719; Abcam). Tissue section images were acquired using an Aperio AT2 scanner (Leica Biosystems) with its integrated microscope and analyzed with ImageJ software (version 1.54p; National Institutes of Health). IHC scoring followed a four-tier system based on the staining intensity: 0, Negative; 1, weakly positive; 2, positive; and 3, strongly positive.

Statistical analysis. Data were processed and analyzed with R (v4.2.2; https://www.r-project.org) and GraphPad Prism 9.0. Statistical significance was evaluated via two-tailed tests. Comparisons between two groups were performed using unpaired Student's t-test for normally distributed data or

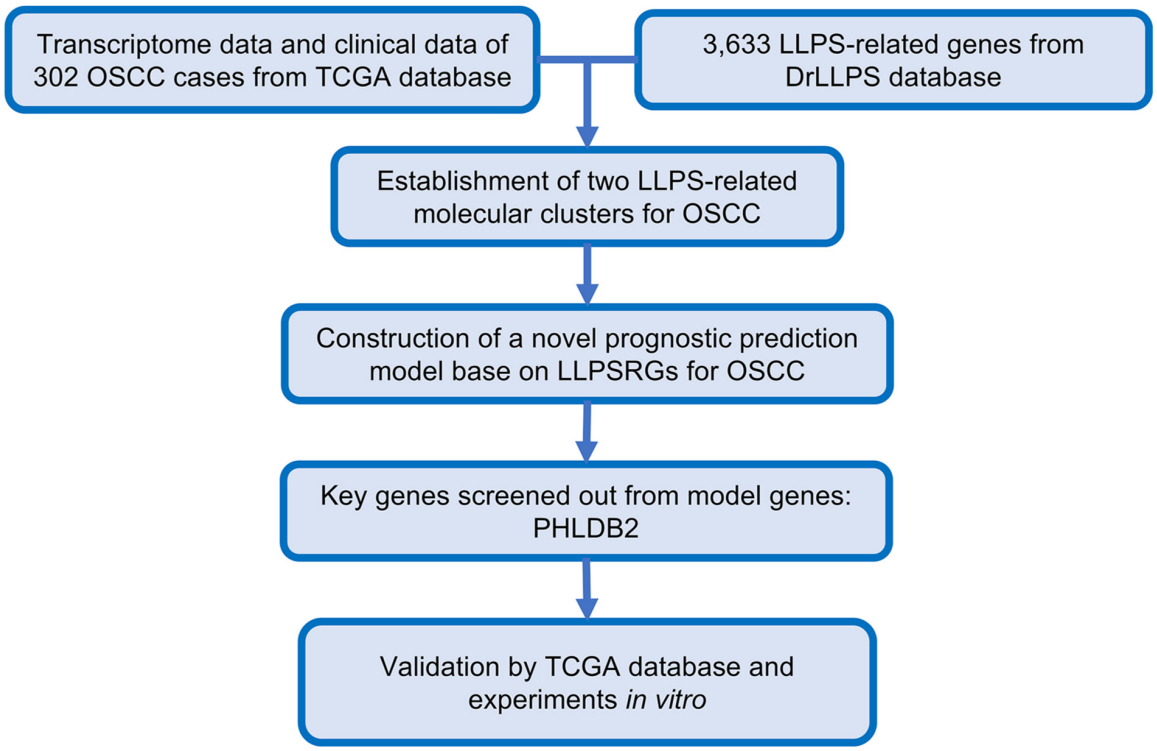

Figure 1. Workflow diagram of the present study. DrLLPS, Data Resource of LLPS; LLPS, liquid-liquid phase separation; LLPSRGs, LLPS-related genes; OSCC, oral squamous cell carcinoma; TCGA, The Cancer Genome Atlas.

Mann-Whitney U tests for non-normally distributed data. Paired comparisons between two groups employed paired Student's t-test for normally distributed data or Wilcoxon signed-rank tests for non-normally distributed data. Multi-group comparisons were analyzed by one-way ANOVA with Tukey's post-hoc testing for normally distributed data with equal variance or Kruskal-Wallis test with Dunn's post-hoc correction for non-normally distributed data. Normality was assessed by the Shapiro-Wilk test and homogeneity of variance was verified using Levene's test. Continuous variables were examined by Pearson's correlation, and categorical variables were evaluated by Spearman's correlation. Analysis of paired tumor-normal tissues in TCGA-OSCC was conducted using the R package 'TCGAplot' (https://github.com/tjhwangxiong/TCGAplot). $P<0.05$ was considered to indicate a statistically significant difference.

Results

Establishment of two LLPS-related molecular clusters and construction of a novel prognostic prediction model based on LLPSRGs for OSCC. The workflow of the present study is illustrated in Fig. 1. Through consensus clustering analysis of 3,633 LLPSRGs from the DrLLPS database of transcriptomics data from 302 OSCC cases in TCGA, the samples were successfully stratified into two biologically distinct molecular clusters, C1 and C2 (Fig. 2A). Evaluation of the CDF curve confirmed optimal consistency and cluster stability at k=2 (Fig. S1A). Further analysis revealed that LLPSRGs were significantly upregulated in C1 compared with in C2 (Fig. 2B), and C1 patients exhibited significantly shorter overall survival (OS; Fig. 2C). GO and KEGG enrichment analyses demonstrated that DEGs in the C1 cluster were predominantly enriched in biological processes associated with tumor progression, including 'cell junction assembly', 'PI3K-Akt signaling pathway' and 'Wnt signaling pathway' (Fig. S1B and C). These findings suggested that dysregulated LLPSRGs may influence OSCC prognosis by modulating key oncogenic pathways.

Based on these insights, seven LLPSRGs significantly associated with OSCC prognosis were identified using Cox proportional hazards regression (Fig. 2D) and their predictive efficacy was further validated via LASSO regression (Fig. 2E). To establish a robust model, TCGA-OSCC cohort was randomly divided into training (n=211) and validation (n=91) groups at a 7:3 ratio. A novel prognostic prediction model was developed through LASSO regression analysis using the training set data, ultimately yielding the following mathematical formula: RiskScore=Exp(SYT1) x 0.126671488410991 + Exp(MYO1B) x 0.116232649674581 + Exp(PHLDB2) x 0.111345681109828 + Exp(CORO2B) x 0.0992669799054353 + Exp(CDH13) x 0.0701283734822018 + Exp(DDX21) x 0.0342177920472229 + Exp(PKLR) x -0.202003545600354. After stratifying TCGA-OSCC patients into high- and low-risk groups, the gene expression heatmap reveals distinct expression patterns of model genes demonstrating clear distinctions between the two subgroups (Fig. 2F).

To validate the predictive performance of the developed model, risk scores were calculated for all patients, with samples stratified into high- and low-risk groups based on median values (Fig. 2G and K). PCA and t-SNE revealed distinct spatial separation between the two groups in gene expression profiles (Fig. S2A-D), confirming the biological discriminative power of the model. Survival analysis demonstrated markedly

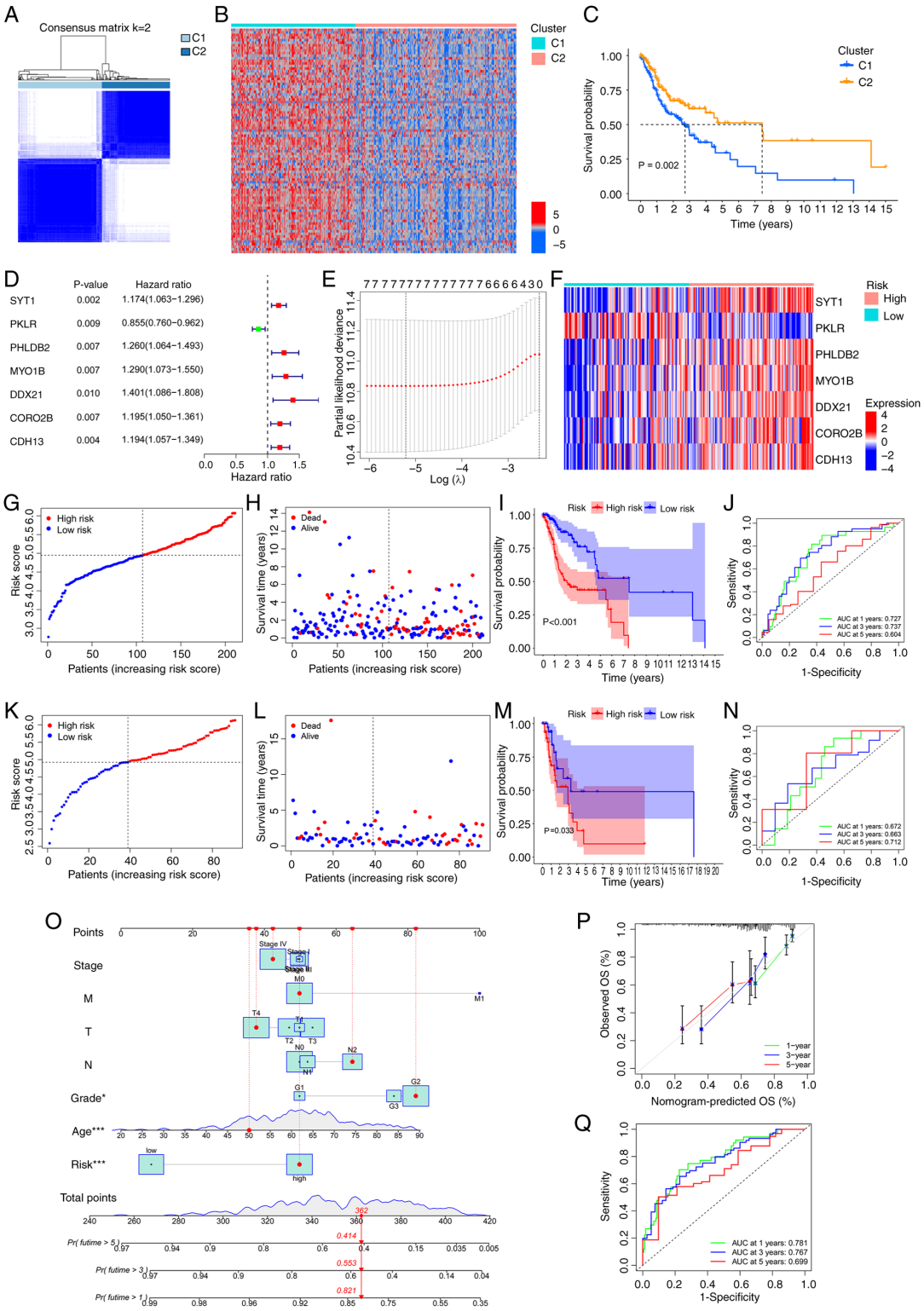

Figure 2. Establishment of two LLPS-related molecular clusters and construction of a novel prognostic prediction model based on LLPSRGs for OSCC. (A) Consensus clustering matrix heatmap illustrating optimal partitioning (k=2) of TCGA-OSCC samples based on LLPSRG expression patterns. (B) Expression profile heatmap of differential genes between C1 and C2 clusters. (C) Kaplan-Meier curves for OS of C1 and C2 clusters. (D) Univariate Cox regression screening identifying seven prognostically significant LLPSRGs. (E) Construction of a prognostic prediction model through LASSO coefficient trajectories with a vertical line indicating optimal λ selection through 10-fold cross-validation. (F) Expression profile heatmap of the seven model genes. Training cohort validation including (G) risk stratification by median cut-off, (H) survival distribution mapping, (I) Kaplan-Meier curves for OS of the high- and low-risk groups, and (J) time-dependent ROC analysis demonstrating predictive accuracy (AUC values for 1, 3 and 5-year survival). Testing cohort validation including (K) risk stratification by median cutoff, (L) survival distribution mapping, (M) Kaplan-Meier curves for OS of the high- and low-risk groups, and (N) time-dependent ROC analysis demonstrating predictive accuracy (AUC values for 1, 3 and 5-year survival). (O) Construction of a prognostic nomogram model integrating risk score with clinical parameters (Tumor-Node-Metastasis stage, histological grade and age). (P) Calibration plots showing concordance between predicted and observed survival probabilities at 1, 3 and 5-year intervals. (Q) Time-dependent ROC analysis demonstrating predictive accuracy (AUC values for 1, 3 and 5-year survival). *P<0.05 and ***P<0.001 by multivariate Cox regression analysis. AUC, area under the curve; LLPS, liquid-liquid phase separation; LLPSRG, LLPS-related gene; OS, overall survival; OSCC, oral squamous cell carcinoma; ROC, receiver operating characteristic; TCGA, The Cancer Genome Atlas.

higher mortality in the high-risk group (Fig. 2H and L) and significantly reduced OS rates compared with those in the low-risk group (Fig. 2I and M). Time-dependent ROC curves showed area under the curve (AUC) values of 0.727, 0.737 and 0.604 for 1-, 3- and 5-year survival predictions in the training set, and 0.672, 0.663 and 0.712 in the validation set, indicating high sensitivity and specificity (Fig. 2J and N).

To enhance clinical applicability, the risk score was integrated with traditional clinicopathological parameters (TNM stage, histological grade and age) to construct a nomogram model (Fig. 2O). Calibration curves demonstrated strong concordance between predicted and observed survival probabilities at 1, 3 and 5 years (Fig. 2P). The nomogram model exhibited significantly improved AUC values compared with the risk score alone (Fig. 2Q), highlighting its superior accuracy in individualized prognosis prediction. These results underscore the potential of the LLPSRG-based prognostic model to refine clinical risk stratification and inform targeted therapeutic strategies for OSCC.

Functional enrichment analysis of DEGs between high- and low-risk groups. To investigate the mechanistic basis of survival disparities between the high- and low-risk cohorts, comparative expression profiling of LLPSRGs across both groups was conducted. The results revealed 401 significantly upregulated genes and 60 downregulated genes in the high-risk group ($P<0.05$; $|log2FC|>1$; Fig. 3A). The MA plot demonstrated no significant association between gene expression levels and fold changes (Fig. 3B), ruling out technical bias as a cause of false-positive results for highly expressed genes. According to the core characteristics of LLPS, proteins capable of phase separation require local critical concentrations and rely on IDRs to promote droplet-like condensate formation. Therefore, the functional properties of upregulated genes were focused on.

Hallmark GSEA based on the MsigDB confirmed that EMT was significantly enriched [normalized enrichment score (NES), 2.45; Fig. 3C]. KEGG pathway analysis further demonstrated significant enrichment of these genes in the 'PI3K-Akt signaling pathway', 'ECM-receptor interaction' and 'focal adhesion' (Fig. 3D), suggesting their potential role in promoting cell migration and invasion through ECM remodeling.

Consistent with the aforementioned findings, GO analysis revealed significant enrichment of upregulated genes in biological processes involving ECM remodeling and cell adhesion regulation (Fig. 3E). Notably, GO enrichment analysis of downregulated genes revealed pronounced enrichment in pathways governing epithelial differentiation and keratinization processes (Fig. 3F), underscoring the suppression of epithelial lineage commitment, which corroborates the previously observed EMT pathway activation.

Expression profile of prognostic model genes in OSCC at a single cell level. To investigate the impact of the seven LLPSRGs in the prognostic model on the malignant progression of OSCC at a single cell level, systematic analyses were conducted using the public scRNA-seq dataset, GSE234933. Primary tumor samples (n=19, total cells=123,094) and metastatic tumor samples (n=8, total cells=38,987) were selected based on clinical information. Risk scores for all cells were calculated using the established prognostic model formula. Results revealed significantly higher risk scores in metastatic tumor cells compared with primary tumor cells (Fig. 4A). When stratifying cells into high- and low-risk groups based on the median risk score, the metastatic tumor group exhibited a significantly higher proportion of high-risk cells (Fig. 4B; 61.9 vs. 44.2% in primary tumors).

Given the aggressive phenotype and elevated risk scores of metastatic cells, subsequent analyses focused on the metastatic cell population. Unsupervised clustering and canonical marker genes were used to annotate major cell types (Fig. 4C), with marker gene expression heatmaps (such as fibroblast marker COL1A1 and cytotoxic T cell marker CD8B) confirming accurate classification (Fig. 4D). Risk profiling across all cell clusters through computing risk model algorithms revealed pronounced risk score enrichment within Uniform Manifold Approximation and Projection (UMAP)-defined tumor cell niches (Fig. 4E), guiding subsequent investigations to focus on tumor cell subpopulations.

Tumor cells were subdivided into the following five functional subtypes: i) Cell cycle; ii) epithelial differentiation; iii) hypoxia; iv) immune suppression; and v) partial (p)EMT, based on canonical markers (Fig. 4F). Heatmaps of subtype marker genes (such as CDC20 marking the cell cycle subtype and KRT5 marking epithelial differentiation) validated classification accuracy (Fig. 4G). Risk scores were calculated across tumor cell subpopulations (Fig. 4H), revealing a pronounced risk elevation in the pEMT subpopulation (Fig. 4I). Consistently, when tumor cells were stratified by median risk score, high-risk tumor cells exhibited a higher proportion of the pEMT subtype (Fig. 4J; 16.2 vs. 10.3% in low-risk), a subtype strongly associated with tumor invasion and metastatic potential (19). Mechanistically aligning with prior pathway enrichment findings, specific activation of the EMT signature pathway was also observed in the pEMT subpopulation (Fig. 4K; NES, 1.39), indicating that the EMT activation detected in bulk transcriptomics analyses predominantly originates from the pEMT subpopulation within tumor cells.

In summary, single-cell analyses demonstrated that high-risk cell populations foster a pro-metastatic environment in OSCC through activation of pEMT tumor cell subpopulations.

LLPS phenomenon of PHLDB2 in OSCC. To delineate core oncogenic drivers among the seven prognostic model genes that drive the malignant progression of OSCC, the GEPIA2 website (20) was used to compare the relative expression of the seven LLPSRGs in TCGA-OSCC (Fig. S3A), prioritizing four highly expressed candidates, MYO1B, DDX21, CDH13 and PHLDB2. RT-qPCR of the seven genes in the OSCC cell lines verified the aforementioned results (Fig. S3B and C). Subsequently, integrative prognostic mapping for TCGA-OSCC by GEPIA2 (Fig. S3D) further refined the key regulator candidates to MYO1B, CDH13 and PHLDB2.

To evaluate their phase separation potential, the amino acid sequences of these proteins were obtained from the UniProt database (https://www.uniprot.org/) and uploaded to the IUPred2A platform (17) to analyze their IDR propensity.

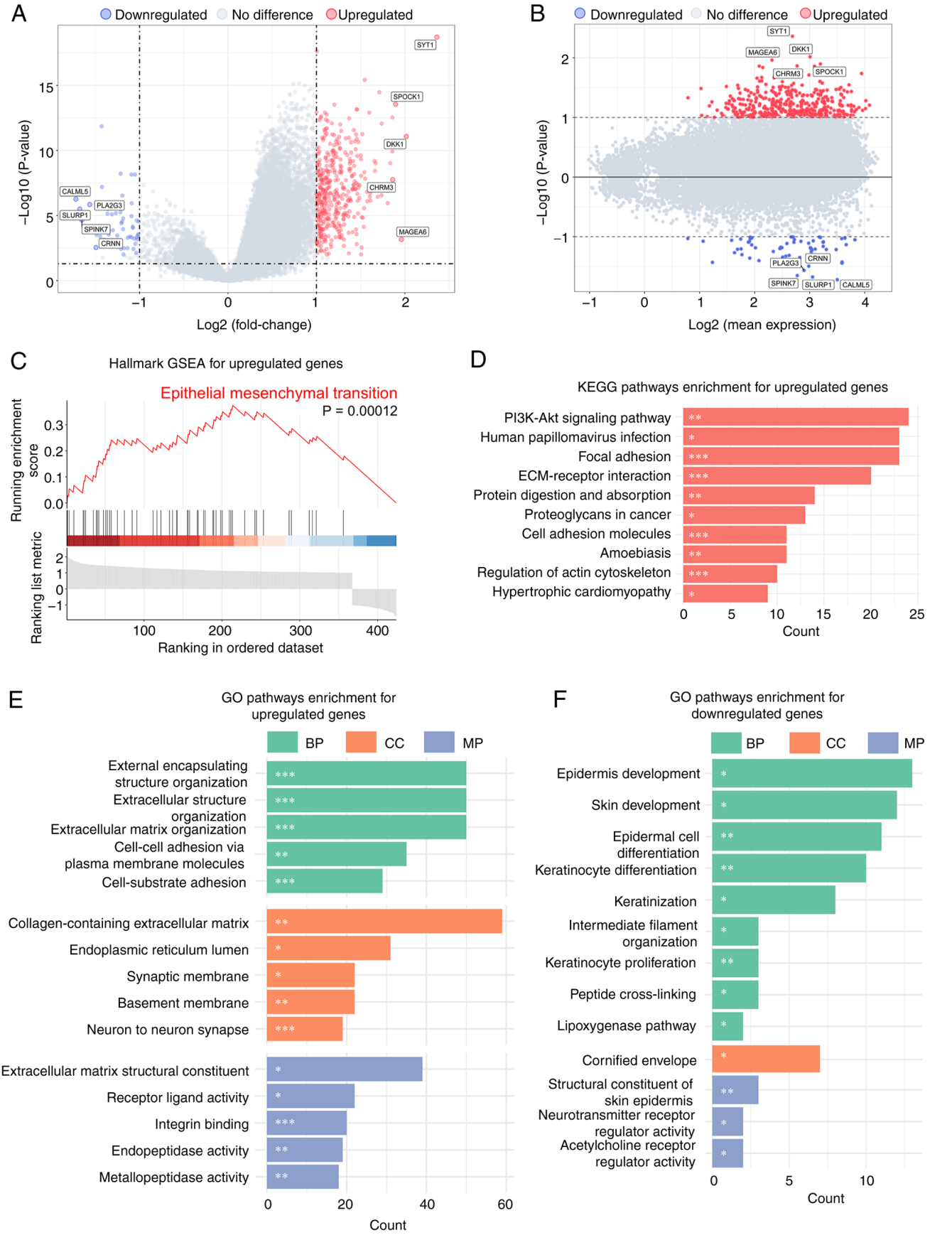

Figure 3. Functional enrichment analysis and tumor microenvironment analysis of DEGs between high- and low-risk groups. (A) DEG analysis identified significant differences between high- and low-risk groups (threshold: P<0.05 and |log2 fold change|>1). (B) Minus-vs.-Add plot quality control of the DEG analysis. (C) Hallmark GSEA revealed enriched pathways in upregulated DEGs. (D) KEGG GSEA identified significant pathways in upregulated DEGs (FDR<0.05). (E) GO GSEA determined biological functions in upregulated DEGs (FDR<0.05). (F) GO GSEA determined biological functions in downregulated DEGs (FDR<0.05). *P<0.05, **P<0.01 and ***P<0.001. DEGs, differentially expressed genes; FDR, false discovery rate; GO, Gene Ontology; GSEA, gene set enrichment analysis; KEGG, Kyoto Encyclopedia of Genes and Genomes.

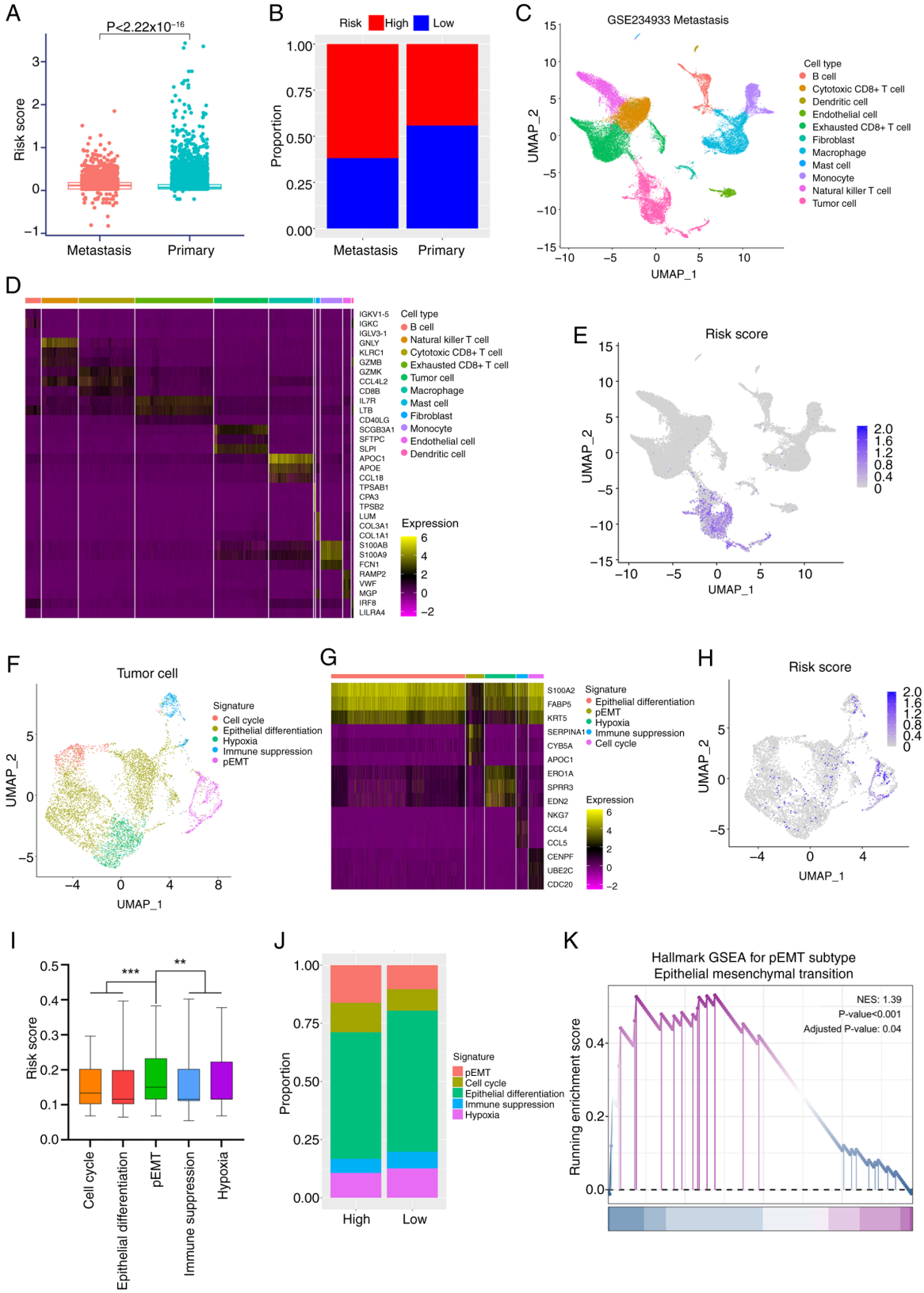

Figure 4. Expression profile of prognostic model genes in oral squamous cell carcinoma at a single cell level. (A) Risk scores of cells in primary and metastatic groups in the GSE234933 dataset based on model gene signatures. (B) Bar plot showing the distribution of high-risk and low-risk cells in the primary and metastatic groups, stratified by median risk score. (C) UMAP visualization of single-cell transcriptomes from the metastatic group in GSE234933, with cell clusters identified by unique gene expression profiles. (D) Heatmap showing the expression of the top three marker genes for each cell cluster. (E) UMAP visualization of the risk score calculated for the cells from the metastatic group. (F) UMAP clustering of the tumor cell subtype in the metastatic group, identified by unique gene expression profiles. (G) Heatmap showing the expression of the top three marker genes for each tumor cell subtype. (H) UMAP visualization of the risk score calculated for the cells of the tumor cell subtype. (I) Risk scores calculated for the cells of the tumor cell subtype. (J) Proportion of tumor cell subtypes in the high- and low-risk groups, stratified by the median risk score. (K) Hallmark GSEA for pEMT tumor cell subpopulation. **P<0.01 and ***P<0.001. GSEA, gene set enrichment analysis; NES, normalized enrichment score; pEMT, partial epithelial-mesenchymal transition; UMAP, Uniform Manifold Approximation and Projection.

The prediction revealed markedly higher phase separation potential for PHLDB2 compared with MYO1B and CDH13 (Figs. 5A, S3E and S3F). In addition, LLPS scoring for PHLDB2, MYO1B and CDH13 by PhaSePred (18) supported the aforementioned results (Figs. 5B, S3G and S3H), prompting further in-depth investigation of PHLDB2.

To validate whether PHLDB2 undergoes LLPS, its ability to form condensates *in vitro* was first examined. In LLPS buffer containing 50 mM NaCl, Alexa Fluor 488-labeled PHLDB2 protein formed phase-separated droplets ranging 2.5-15 μm in diameter, with droplet size positively associated with protein concentration (2.5-15 μM; Fig. 5C) and inversely associated with NaCl concentration (50-500 mM; Fig. 5D). Notably, live-cell imaging of the SCC1 OSCC cell line transfected with PHLDB2-EGFP plasmids demonstrated the formation of cytoplasmic droplets (Fig. 5E). FRAP assays further confirmed the liquid-like properties of these condensates, with fluorescence recovering to 31.4% at 5 sec, 52.6% at 30 sec and 62.7% at 60 sec post-bleaching (Fig. 5F and G). These results conclusively demonstrated that PHLDB2 forms LLPS condensates in OSCC cells.

Promoting effects of PHLDB2 on proliferation, stemness and invasion in OSCC cell lines. To investigate the regulatory role of PHLDB2 in the biological behavior of OSCC cells, two sequence-specific siRNAs were designed to knockdown PHLDB2 expression in SCC1 and HSC3 cell lines via transient transfection. RT-qPCR and western blotting results demonstrated that both siRNAs significantly reduced PHLDB2 mRNA and protein levels (Fig. 6A and B), confirming the high efficiency and specificity of the knockdown system.

CCK-8 assays revealed a significant decline in proliferation rates over time in the PHLDB2 knockdown groups (Fig. 6C and D). Tumor-sphere formation assays further showed that the number of tumor-spheres and their average diameter were significantly reduced in the knockdown groups compared with those in the control groups (Fig. 6E-H). Limiting dilution assays confirmed impaired self-renewal capacity of tumor stem cells following PHLDB2 knockdown (Fig. 6I and J). Additionally, colony formation assays indicated a significant decrease in colony numbers in the knockdown groups (Fig. 6K and L), suggesting the critical role of PHLDB2 in maintaining tumor stemness.

For tumor invasion, Transwell assays showed a significant reduction in matrix gel-penetrating cells in the PHLDB2 knockdown groups (Fig. 6M and N). Wound healing assays further revealed decreased wound closure rates in knockdown cells (Fig. 6O-R). These results systematically demonstrated that PHLDB2 promotes OSCC malignant progression by enhancing cell proliferation, stemness maintenance and invasive potential.

Exploration of the molecular mechanisms of PHLDB2 promoting the malignant characteristics of OSCC. To elucidate the molecular mechanisms by which PHLDB2 promotes malignant phenotypes in OSCC cells, a multi-dimensional data cross-validation strategy was employed that systematically compared RNA-seq data from PHLDB2 knockdown experiments with transcriptomics data from TCGA-OSCC cohort. For TCGA-OSCC public data, patients were stratified into high- and low-expression groups based on PHLDB2 levels, followed by differential gene analysis identifying 3,147 distinctively upregulated genes and 15,398 distinctively downregulated genes in the PHLDB2 low-expression group (Fig. 7A). Subsequent Hallmark and GO GSEA based on MsigDB were performed on these DEGs, collectively named the PHLDB2-TCGA pathway enrichment results (Fig. 7C). SCC1 cells were transiently transfected with PHLDB2-si1 siRNA to knockdown PHLDB2 expression, and three biological replicates were conducted for both the experimental group (PHLDB2-si) and the control group (control-si), followed by RNA-seq. Differential expression analysis (thresholds, $P<0.05$ and $|log2FC|>1$) confirmed reliable knockdown efficiency of PHLDB2-si, identifying 80 distinctively upregulated genes and 360 distinctively downregulated genes in the PHLDB2 knockdown group (Fig. 7B). Subsequent Hallmark and GO GSEA based on MsigDB were performed on these DEGs, collectively named the PHLDB2-RNAseq pathway enrichment results (Fig. 7C).

To delineate core pathway convergence in PHLDB2-deficient molecular contexts, a cross-dataset intersection of the PHLDB2-RNAseq and PHLDB2-TCGA pathway enrichment results was performed (Fig. 7C). Consensus pathway analysis of the intersecting 152 molecular signatures demonstrated significant suppression of the Hallmark EMT gene set in PHLDB2-depleted samples (NES, -2.833; false discovery rate, 0.023; Fig. 7D), consistent with the Hallmark enrichment results from prognostic model genes (Fig. 3C). Western blot validation of core EMT markers confirmed these findings (Fig. S4), showing decreased N-cadherin and vimentin protein levels accompanied by increased E-cadherin expression in the PHLDB2-si groups compared with those in the control-si groups. GO enrichment analysis further demonstrated that pathways related to ECM remodeling and the cell-substrate junction including 'extracellular structure organization', 'extracellular matrix organization', 'cell-substrate junction assembly' and 'cell-substrate junction organization', were markedly downregulated (Fig. 7E), mechanistically implicating that PHLDB2 depletion impaired EMT activation dynamics in OSCC.

To elucidate the molecular mechanisms underlying PHLDB2-mediated EMT regulation, KEGG GSEA was conducted for downregulated genes in PHLDB2-depleted samples, which revealed significant enrichment of the 'PI3K-Akt signaling pathway' (Fig. 7F), recapitulating the pathway convergence pattern observed in prior prognostic model gene signatures. Subsequent expression profiling of core PI3K-Akt signaling components in PHLDB2-knockdown models demonstrated marked downregulation of PIK3CA (Fig. 7G). Further validation through RT-qPCR in PHLDB2-knockdown OSCC cell lines confirmed the transcriptional repression of PIK3CA (Fig. 7H and I). Previous research has identified PIK3CA as a critical molecular regulator of EMT activation (24,25). Integrated analysis of the multidimensional datasets in the present study revealed that PHLDB2-mediated upregulation of PIK3CA may constitute a novel mechanistic axis driving EMT progression in OSCC pathogenesis.

High expression of PHLDB2 is associated with a poorer prognosis for patients with OSCC. To clarify the expression characteristics and clinical significance of PHLDB2 in OSCC

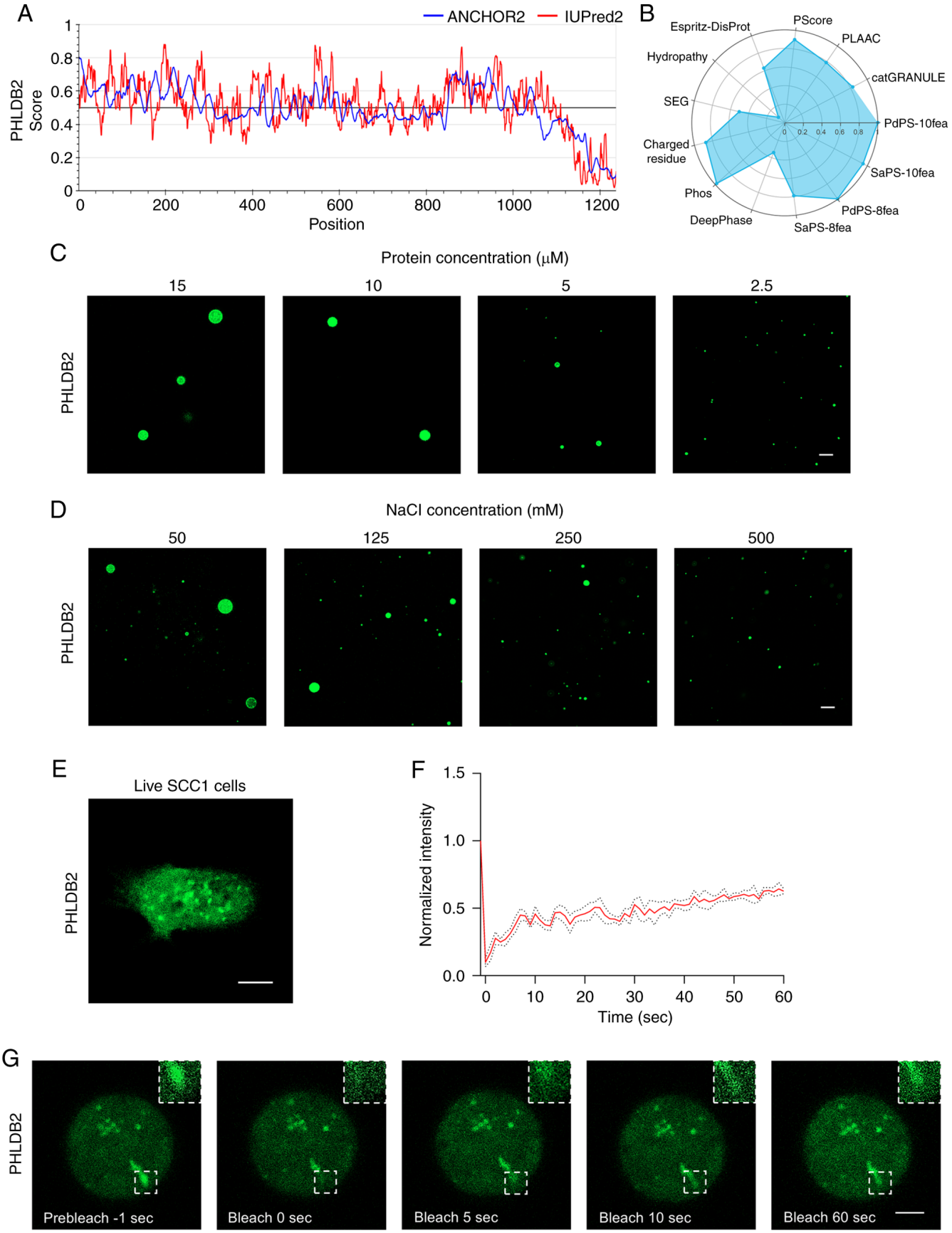

Figure 5. LLPS phenomenon of PHLDB2 in OSCC. (A) Prediction of disordered protein regions (IUPred2) and disordered binding motifs (ANCHOR2) in PHLDB2 via the IUPred2A platform. (B) LLPS propensity scoring of PHLDB2 using PhaSePred. *In vitro* droplet assay images of Alexa Fluor 488-labeled PHLDB2 condensates under increasing (C) protein or (D) NaCl concentrations (scale bar, 10 μm). (E) EGFP-PHLDB2 plasmid-transfected SCC1 cells showing intracellular droplet formation (scale bar, 10 μm). (F) FRAP-based quantification of normalized fluorescence intensity in EGFP-PHLDB2 condensates within live OSCC cells. (G) FRAP recovery time-lapse imaging of EGFP-PHLDB2 droplets in live OSCC cells (scale bar, 10 μm). FRAP, fluorescence recovery after photobleaching; LLPS, liquid-liquid phase separation; OSCC, oral squamous cell carcinoma.

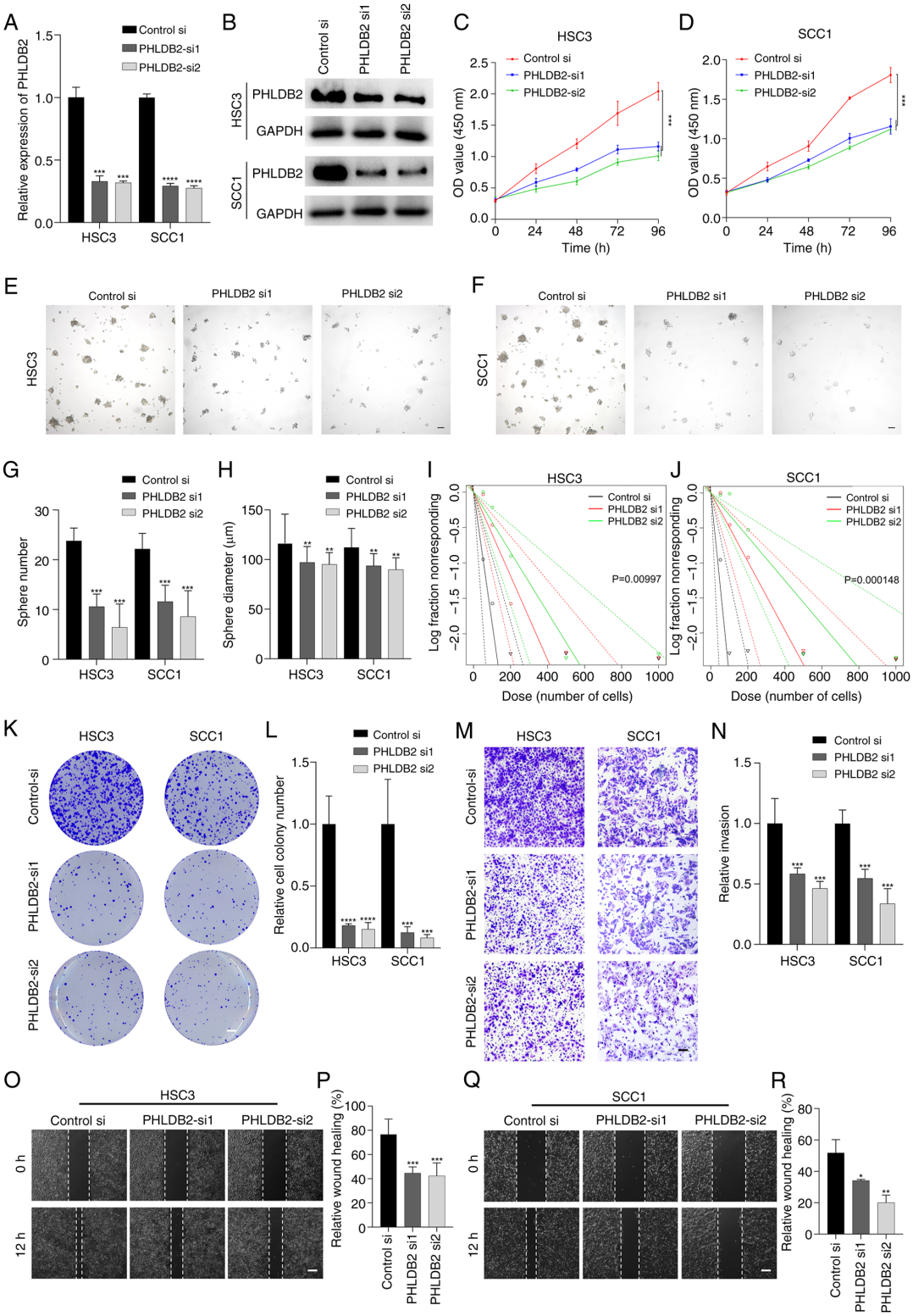

Figure 6. Promoting effects of PHLDB2 on proliferation, stemness, invasion and metastasis in OSCC cell lines. (A) PHLDB2 mRNA levels were decreased in OSCC cells transfected with PHLDB2-targeting siRNAs (si1/si2). ***P<0.001, ****P<0.0001 vs. control-si. (B) Western blotting confirmed PHLDB2 protein knockdown following siRNA transfection. OD values demonstrated changes in (C) HSC3 cells and (D) SCC1 cells upon PHLDB2 depletion. ***P<0.001. Tumor spheres formed in (E) HSC3 cells and (F) SCC1 cells. Scale bar, 100 μm. (G) Sphere number decreased in PHLDB2-knockdown HSC3/SCC1 cells. ***P<0.001 vs. control-si. (H) Sphere diameter decreased in PHLDB2-knockdown HSC3/SCC1 cells. **P<0.01 vs. control-si. Sphere-forming capacity decreased in (I) HSC3 cells and (J) SCC1 cells with PHLDB2 knockdown. (K) Representative image of colony formation assays showed reduction in PHLDB2-knockdown HSC3/SCC1 cells vs. control. Scale bar, 3 mm. (L) Quantification of colony formation assays showed reduction in PHLDB2-knockdown HSC3/SCC1 cells. ***P<0.001, ****P<0.0001 vs. control-si. (M) Representative image of invasion assays indicated suppression in PHLDB2-knockdown HSC3/SCC1 cells. Scale bar, 50 μm. (N) Quantification of invasion assays indicated suppression in PHLDB2-knockdown HSC3/SCC1 cells. ***P<0.001 vs. control-si. (O) Representative image of wound healing assays indicated depletion of migratory capacity in PHLDB2-knockdown HSC3 cells vs. control. Scale bar, 100 μm. (P) Wound healing assays indicated depletion of migratory capacity in PHLDB2-knockdown HSC3 cells. ***P<0.001 vs. control-si. (Q) Quantification of wound healing assays indicated depletion of migratory capacity in PHLDB2-knockdown SCC1 cells vs. control. Scale bar, 100 μm. (R) Wound healing assays indicated depletion of migratory capacity in PHLDB2-knockdown SCC1 cells. *P<0.05, **P<0.01 vs. control-si. OSCC, oral squamous cell carcinoma; si, small interfering.

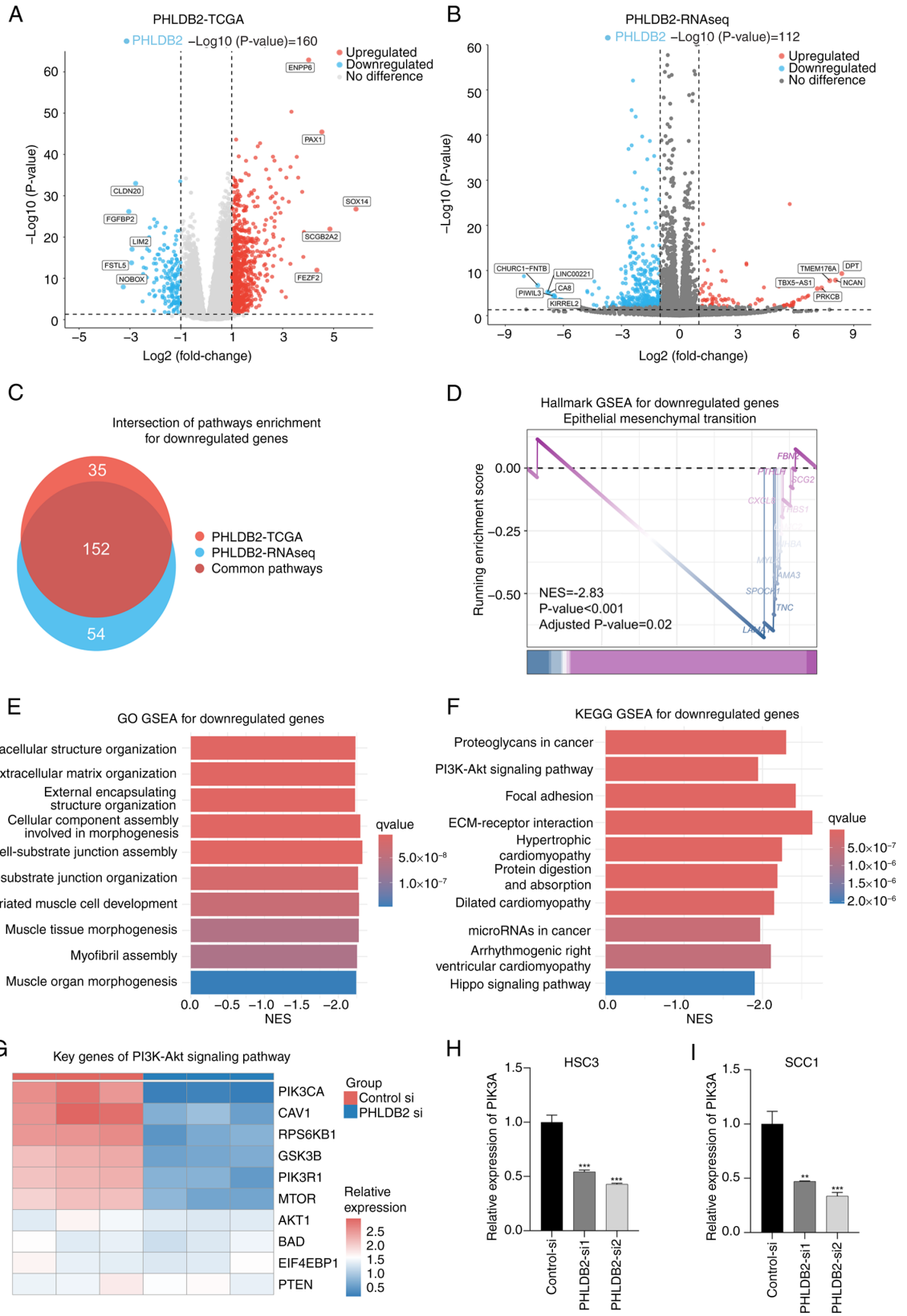

Figure 7. Exploration of the molecular mechanisms of PHLDB2 promoting the malignant characteristics of OSCC. (A) Differential gene analysis identified differentially expressed genes between PHLDB2 low- and high-expression groups in TCGA-OSCC cohort. Threshold: P<0.05 and |log2FC|>1. (B) Differential gene analysis identified differentially expressed genes between the PHLDB2 knockdown group and the control group. Thresholds: P<0.05 and |log2FC|>1. (C) Intersection analysis revealed downregulated pathways shared between PHLDB2-RNAseq and PHLDB2-TCGA enrichment profiles. (D) Integrated Hallmark pathway analysis demonstrated enriched pathway for downregulated genes. (E) Integrated GO pathway analysis identified enriched biological terms for downregulated genes. (F) Integrated KEGG pathway analysis showed enriched pathways for downregulated genes. (G) Heatmap displayed expression patterns of PI3K-Akt signaling pathway genes in PHLDB2-knockdown vs. control groups. Reverse transcription-quantitative PCR indicated reduced PIK3CA expression in PHLDB2-depleted (H) HSC3 and (I) SCC1 cells. **P<0.01, ***P<0.001 vs. control-si. GO, Gene Ontology; GSEA, gene set enrichment analysis; KEGG, Kyoto Encyclopedia of Genes and Genomes; NES, normalized enrichment score; OSCC, oral squamous cell carcinoma; RNAseq, RNA sequencing; TCGA, The Cancer Genome Atlas; MsigDB, Molecular Signatures Database; si, small interfering.

clinical samples, multicenter data were systemically integrated. Analysis of TCGA database revealed that PHLDB2 mRNA expression was significantly higher in OSCC tumor tissues (n=302) compared with that in adjacent tissues (n=67; Fig. 8A), with consistent differences observed in paired tumor-adjacent samples (Fig. 8B). This trend was further validated in the independent cohort GSE213862 (n=43), where PHLDB2 expression in OSCC tissues was significantly elevated compared with that in normal mucosal tissues from healthy individuals (Fig. 8C). Notably, analysis of TCGA-OSCC cohort demonstrated that PHLDB2 expression was significantly higher in advanced-stage tumors (T3/T4) compared with that in early-stage tumors (T1/T2) (Fig. 8D), and patients with high PHLDB2 expression had significantly shorter OS compared with that in the patients with low PHLDB2 expression (Fig. 8E).

To further validate protein-level expression characteristics, IHC analysis was performed on an OSCC cohort (n=51) from the Hospital of Stomatology, SYSU. Negative control experiments using non-specific IgG demonstrated assay specificity (Fig. S5). Results indicated significantly higher PHLDB2 protein expression in tumor tissues compared with those in adjacent normal tissues (Fig. 8F-H). Additionally, high PHLDB2 expression was significantly associated with lymph node metastasis (Fig. 8I) and poor tumor differentiation (G2/3 vs. G1; Fig. 8J). These data collectively suggested that elevated PHLDB2 expression may be closely linked to malignant progression and poor prognosis in OSCC.

Discussion

Previous studies on LLPSRGs and OSCC have primarily focused on characterizing phase separation phenomena of established oncogenes (such as FOSL1 and DAZAP1) (26,27); however, to the best of our knowledge, the systematic exploration of their prognostic value remains unreported. Notably, prognostic models based on LLPSRGs have demonstrated efficacy in stratifying patient survival in ovarian (12), breast (13) and bladder cancer (14), yet this strategy remains unexplored in OSCC. The present study innovatively integrated LLPS mechanism exploration with prognostic model construction, establishing the first OSCC-specific LLPSRG prognostic prediction model, by conducting Cox and LASSO regression analyses on LLPSGs and survival rate of TCGA-OSCC cohort. Through rigorous bioinformatics screening and experimental validation, the independent prognostic value of the key gene PHLDB2 was investigated, and to the best of our knowledge, the first experimental evidence that the PHLDB2 protein exhibits spontaneous LLPS in OSCC cells was provided. This discovery addresses the research gap regarding LLPSRGs in OSCC prognostic assessment systems.

It is critical to emphasize the screening strategy of the present study. Although the DrLLPS database provides 3,633 proteins predicted to have LLPS potential, these predictions require experimental validation of their biological functions (28). To enhance result reliability, genes with high scores across multiple phase separation prediction platforms [such as IUPred2A (19) and PhaSepDB (20)] were prioritized during the selection of key model genes, ultimately identifying PHLDB2. Notably, as well as PHLDB2, the other six core genes (SYT1, MYO1B, CORO2B, CDH13, DDX21 and PKLR) included in the present prognostic model have partial functional annotations in tumor biology, but their LLPS-related mechanisms and roles in OSCC malignant progression have not yet been elucidated.

Specifically, SYT1 was associated with poor prognosis as a high-risk gene in the present model, contradicting its tumor-suppressive role observed by Shi *et al* (29) in colorectal cancer. Considering the canonical function of SYT1 in neurotransmitter release regulation as a synaptotagmin family member, and previous findings that neural pathways influence tumor progression through diverse mechanisms (30-32), it was hypothesized that SYT1 may activate pro-oncogenic signaling via phase-separated condensates at neural synapse-related sites. This hypothesis requires validation through co-localization experiments and neural co-culture models. MYO1B has been linked to poor prognosis in head and neck squamous cell carcinoma (HNSCC), glioma and colorectal cancer (33-36). Its oncogenic role in HNSCC has been shown to involve regulation by microRNA (miRNA)-145-3p (33), yet whether miRNA-MYO1B interactions involve LLPS warrants further investigation. While CORO2B and CDH13 exhibit oncogenic properties in esophageal squamous cell carcinoma (37) and renal cancer (38), their molecular mechanisms remain unconnected to LLPS, offering new research directions. Notably, the high-risk association of DDX21 in the present model aligns with its function in colorectal cancer. Specifically, Gao *et al* (39) demonstrated that DDX21 activates EMT pathways through LLPS-dependent chromatin remodeling, suggesting a conserved metastatic mechanism in OSCC. By contrast, the negative association between the low expression and poor prognosis (negative risk coefficient) of PKLR contradicts the majority of reports (40-42), potentially attributable to the unique metabolic microenvironment of OSCC or dynamic changes in the phase-separated states of PKLR, necessitating further investigation. While SYT1, CORO2B, CDH13, DDX21 and PKLR lack extensive prior links to OSCC, their strong prognostic value in the present analysis warrants further mechanistic exploration.

To the best of our knowledge, the present study is the first to reveal the critical role of PHLDB2 as an LLPS driver in OSCC, yet the molecular mechanisms by which it regulates downstream signaling via LLPS require deeper exploration. Notably, the findings of the present study do not directly establish a causal relationship between PHLDB2-mediated LLPS and EMT/invasive phenotypes, which requires validation, potentially through the following mechanistic studies: i) Generation of LLPS-deficient PHLDB2 mutants (targeting IDRs/key domains) and validation of the loss of potential condensate formation outside and in cells, followed by assessment of the effects of wild-type vs. mutant PHLDB2 on EMT markers and biofunction in OSCC cells. ii) Identification of proteins specifically recruited into PHLDB2 condensates using proximity labeling and co-immunoprecipitation coupled with mass spectrometry, and assessment of the functional roles of identified partners and oncogenic pathways activated by LLPS. iii) Comparison of tumor growth/metastasis of cells expressing wild-type vs. mutant PHLDB2 in mouse models.

As a pleckstrin homology domain protein family member, PHLDB2 has been reported to participate in tumor metastasis by regulating cytoskeletal rearrangement and focal adhesion

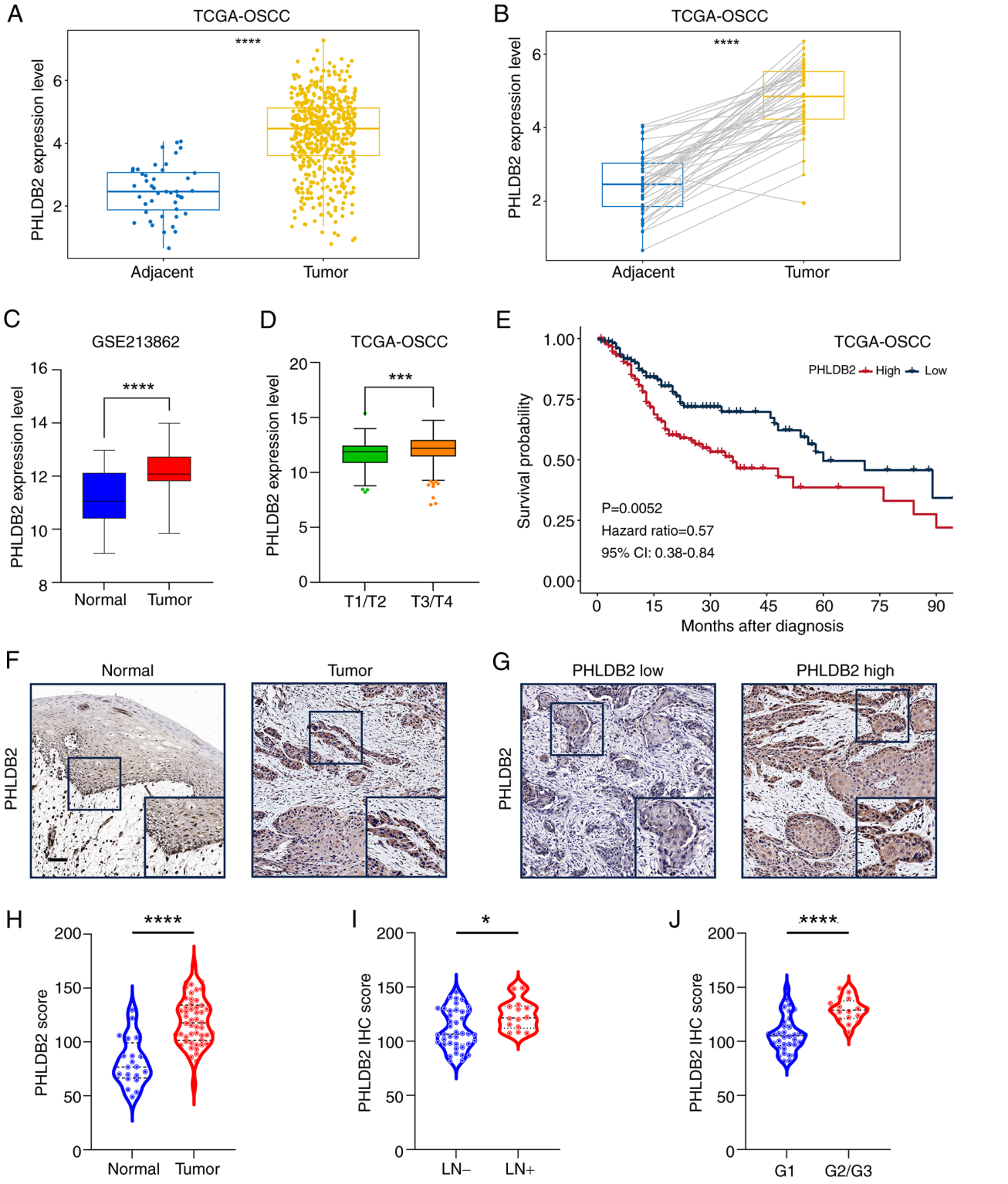

Figure 8. High expression of PHLDB2 is associated with a poorer prognosis for patients with OSCC. (A) Expression levels of PHLDB2 in tumor and normal tissues from TCGA-OSCC cohort. (B) PHLDB2 expression in paired tumor and normal samples from TCGA-OSCC cohort. (C) PHLDB2 levels in OSCC tissues and normal mucosa in the GSE213862 cohort. (D) PHLDB2 expression in early-stage (T1/T2) and late-stage (T3/T4) tumors from TCGA-OSCC . (E) Survival comparison between the PHLDB2 high and low expression groups in TCGA-OSCC. (F and G) IHC staining of PHLDB2 in tumor and matched normal tissues (Sun Yat-Sen University cohort; scale bar, 50 μm). Semi-quantitative IHC analysis of (H) tumor vs. normal tissues; (I) LN^+ vs. LN^- tissues ; and (J) G1 vs. G2/G3 tissues. *P<0.05, ***P<0.001 and ****P<0.0001. CI, confidence interval; IHC, immunohistochemical; LN, lymph node metastasis; OSCC, oral squamous cell carcinoma; TCGA, The Cancer Genome Atlas.

dynamics, with established links to EMT in OSCC (43,44), colorectal cancer (45) and gastric cancer (46). Building on the discovery of the spontaneous LLPS condensate formation of PHLDB2 in OSCC cells, the following novel hypothesis was proposed: PHLDB2 may enhance EMT and metastatic efficacy through a phase separation-dependent 'molecular condensation'

mechanism, locally enriching and activating cytoskeletal regulators and PI3K-Akt signaling effectors in microenvironments, such as leading-edge pseudopodia or invasive protrusions. This mechanism could explain why traditional gene expression analysis inadequately captures the oncogenic effects of PHLDB2, as its biological impact may depend heavily on spatiotemporally specific protein interaction networks mediated by LLPS. To address these scientific questions, subsequent research should focus on the following: i) Interactome validation whereby core interacting proteins within PHLDB2 condensates are systematically screened using co-immunoprecipitation coupled with mass spectrometry, emphasizing co-localization patterns of cytoskeletal regulators and PI3K-Akt pathway components. ii) Phase separation domain analysis whereby IDR deletion or phosphorylation site mutants are constructed, combined with FRAP and *in vitro* reconstitution experiments, to define the necessity of the phase separation capability of PHLDB2 for its pro-metastatic function and PI3K-Akt pathway activation. iii) Spatiotemporal dynamics tracking whereby super-resolution live-cell imaging is employed to observe real-time formation-dissolution kinetics of PHLDB2 condensates at migration fronts and their co-evolution with cytoskeletal regulators and PI3K-Akt pathway components. iv) PI3K-Akt condensate crosstalk involving validation of whether PHLDB2 scaffolds PI3K-Akt complexes via LLPS by assessing co-condensation with PIP3-Akt using dual-color imaging, testing functional rescue of EMT phenotypes upon PI3K-Akt inhibition in PHLDB2-overexpressing cells, and mapping PIK3CA-binding capacity of PH domain mutants with impaired phase separation. These investigations could uncover the novel role of LLPS as a 'molecular accelerator' in tumor cell plasticity regulation, providing a theoretical foundation for developing anti-metastatic therapies targeting phase separation processes.

In conclusion, the present study pioneered the integration of LLPS mechanistic investigation with prognostic model development, establishing the first LLPSRG prognostic prediction model specifically for OSCC. By combining comprehensive bioinformatics screening with experimental validation, the independent prognostic significance of the key gene PHLDB2 was confirmed and the first experimental evidence demonstrating the spontaneous LLPS behavior of the PHLDB2 protein in OSCC cells was provided. This discovery fills a critical knowledge gap regarding LLPSRGs within OSCC prognostic evaluation frameworks.

Acknowledgements

Not applicable.

Funding

This work was funded by The National Natural Science Foundation of China (grant nos. 82373015 and 82403204).

Availability of data and materials

The data generated in the present study may be requested from the corresponding author. The RNA-seq generated in the present study may be found in the NCBI SRA database, under accession number PRJNA1274177 or at the following URL: https://www.ncbi.nlm.nih.gov/bioproject/PRJNA1274177, with data of control-si group in SRX29112934 at the following URL: https://www.ncbi.nlm.nih.gov/sra/SRX29112934[accn] and data of PHLDB2-si group in SRX29112935 at the following URL: https://www.ncbi.nlm.nih.gov/sra/SRX29112935[accn].

Authors' contributions

KC and YW conceptualized and validated the present study, performed the study investigation and methodology, and wrote the original draft of the manuscript. JC performed data acquisition and validation, and performed the investigation. QL performed the formal analysis and obtained the resources. XL performed data acquisition and validation. WW conceptualized and supervised the study, acquired the funding and reviewed and edited the manuscript. JH conceptualized and supervised the study, acquired the funding, performed project administration, and reviewed and edited the manuscript. KC and YW confirm the authenticity of all the raw data. All authors read and approved the final version of the manuscript.

Ethics approval and consent to participate

The present study received approval from the ethics committee of the Hospital of Stomatology, Sun Yat-sen University (Guangzhou, China; approval no. KQEC202013) and all participants provided written informed consent.

Patient consent for publication

Not applicable.

Competing interests

The authors declare that they have no competing interests.

References

1. Bray F, Laversanne M, Sung H, Ferlay J, Siegel RL, Soerjomataram I and Jemal A: Global cancer statistics 2022: GLOBOCAN estimates of incidence and mortality worldwide for 36 cancers in 185 countries. CA Cancer J Clin 74: 229-263, 2024.
2. Cramer JD, Burtness B, Le QT and Ferris RL: The changing therapeutic landscape of head and neck cancer. Nat Rev Clin Oncol 16: 669-683, 2019.
3. Alberti S, Gladfelter A and Mittag T: Considerations and challenges in studying liquid-liquid phase separation and biomolecular condensates. Cell 176: 419-434, 2019.
4. Tong X, Tang R, Xu J, Wang W, Zhao Y, Yu X and Shi S: Liquid-liquid phase separation in tumor biology. Signal Transduct Target Ther 7: 221, 2022.
5. Mehta S and Zhang J: Liquid-liquid phase separation drives cellular function and dysfunction in cancer. Nat Rev Cancer 22: 239-252, 2022.
6. Zheng LW, Liu CC and Yu KD: Phase separations in oncogenesis, tumor progressions and metastasis: A glance from hallmarks of cancer. J Hematol Oncol 16: 123, 2023.
7. Blackburn EH: Structure and function of telomeres. Nature 350: 569-573, 1991.
8. Zhang H, Zhao R, Tones J, Liu M, Dilley RL, Chenoweth DM, Greenberg RA and Lampson MA: Nuclear body phase separation drives telomere clustering in ALT cancer cells. Mol Biol Cell 31: 2048-2056, 2020.
9. Lu Y, Wu T, Gutman O, Lu H, Zhou Q, Henis YI and Luo K: Phase separation of TAZ compartmentalizes the transcription machinery to promote gene expression. Nat Cell Biol 22: 453-464, 2020.

10. Cheng Y, Xie W, Pickering BF, Chu KL, Savino AM, Yang X, Luo H, Nguyen DT, Mo S, Barin E, *et al*: N^6-methyladenosine on mRNA facilitates a phase-separated nuclear body that suppresses myeloid leukemic differentiation. Cancer Cell 39: 958-972.e8, 2021.
11. Tulpule A, Guan J, Neel DS, Allegakoen HR, Lin YP, Brown D, Chou YT, Heslin A, Chatterjee N, Perati S, *et al*: Kinase-mediated RAS signaling via membraneless cytoplasmic protein granules. Cell 184: 2649-2664.e18, 2021.
12. Qiu Y, Pan M and Chen X: A liquid-liquid phase separation-related gene signature as prognostic biomarker for epithelial ovarian cancer. Front Oncol 11: 671892, 2021.
13. Yu-Qing H, Peng-Ping L, Ke S, Ke-Xing Y, Wei-Jun Z and Zhen-Yu W: Comprehensive analysis of liquid-liquid phase separation-related genes in prediction of breast cancer prognosis. Front Genet 13: 834471, 2022.
14. Sun L, Liu XP, Yan X, Wu S, Tang X, Chen C, Li G, Hu H, Wang D and Li S: Identification of molecular subtypes based on liquid-liquid phase separation and cross-talk with immunological phenotype in bladder cancer. Front Immunol 13: 1059568, 2022.
15. Chatterjee A, Chaudhary A, Ghosh A, Arun P, Mukherjee G, Arun I, Maitra A, Biswas N and Majumder PP: Overexpression of CD73 is associated with recurrence and poor prognosis of gingivobuccal oral cancer as revealed by transcriptome and deep immune profiling of paired tumor and margin tissues. Cancer Med 12: 16774-16787, 2023.
16. Wilkerson MD and Hayes DN: ConsensusClusterPlus: A class discovery tool with confidence assessments and item tracking. Bioinformatics 26: 1572-1573, 2010.
17. Love MI, Huber W and Anders S: Moderated estimation of fold change and dispersion for RNA-seq data with DESeq2. Genome Biol 15: 550, 2014.
18. Bill R, Wirapati P, Messemaker M, Roh W, Zitti B, Duval F, Kiss M, Park JC, Saal TM, Hoelzl J, *et al*: CXCL9:SPP1 macrophage polarity identifies a network of cellular programs that control human cancers. Science 381: 515-524, 2023.
19. Tang Z, Kang B, Li C, Chen T and Zhang Z: GEPIA2: An enhanced web server for large-scale expression profiling and interactive analysis. Nucleic Acids Res 47: W556-W560, 2019.
20. Mészáros B, Erdos G and Dosztányi Z: IUPred2A: context-dependent prediction of protein disorder as a function of redox state and protein binding. Nucleic Acids Res 46: W329-W337, 2018.
21. Hou C, Wang X, Xie H, Chen T, Zhu P, Xu X, You K and Li T: PhaSepDB in 2022: Annotating phase separation-related proteins with droplet states, co-phase separation partners and other experimental information. Nucleic Acids Res 51: D460-D465, 2023.
22. Livak KJ and Schmittgen TD: Analysis of relative gene expression data using real-time quantitative PCR and the 2(-Delta Delta C(T)) method. Methods 25: 402-408, 2001.
23. Lydiatt WM, Patel SG, O'Sullivan B, Brandwein MS, Ridge JA, Migliacci JC, Loomis AM and Shah JP: Head and Neck cancers-major changes in the American Joint Committee on cancer eighth edition cancer staging manual. CA Cancer J Clin 67: 122-137, 2017.
24. Coussy F, El Botty R, Lavigne M, Gu C, Fuhrmann L, Briaux A, de Koning L, Dahmani A, Montaudon E, Morisset L, *et al*: Combination of PI3K and MEK inhibitors yields durable remission in PDX models of PIK3CA-mutated metaplastic breast cancers. J Hematol Oncol 13: 13, 2020.
25. Jeong YG, Katuwal NB, Kang MS, Ghosh M, Hong SD, Park SM, Kim SG, Kim TH and Moon YW: Combined PI3K inhibitor and eribulin enhances anti-tumor activity in preclinical models of paclitaxel-resistant, PIK3CA-mutated endometrial cancer. Cancers (Basel) 15: 4887, 2023.
26. Zhang J, Ni Z, Zhang Y, Guo Y, Zhai R, Wang M, Gong Z, Wang M, Zeng F, Gu Z, *et al*: DAZAP1 phase separation regulates mitochondrial metabolism to facilitate invasion and metastasis of oral squamous cell carcinoma. Cancer Res 84: 3818-3833, 2024.
27. Wang W, Yun B, Hoyle RG, Ma Z, Zaman SU, Xiong G, Yi C, Xie N, Zhang M, Liu X, *et al*: CYTOR facilitates formation of FOSL1 phase separation and super enhancers to drive metastasis of tumor budding cells in head and neck squamous cell carcinoma. Adv Sci (Weinh) 11: e2305002, 2024.
28. Ning W, Guo Y, Lin S, Mei B, Wu Y, Jiang P, Tan X, Zhang W, Chen G, Peng D, *et al*: DrLLPS: A data resource of liquid-liquid phase separation in eukaryotes. Nucleic Acids Res 48 (D1): D288-D295, 2020.
29. Shi J, Li W, Jia Z, Peng Y, Hou J, Li N, Meng R, Fu W, Feng Y, Wu L, *et al*: Synaptotagmin 1 suppresses colorectal cancer metastasis by inhibiting ERK/MAPK signaling-mediated tumor cell pseudopodial formation and migration. Cancers (Basel) 15: 5282, 2023.
30. Balood M, Ahmadi M, Eichwald T, Ahmadi A, Majdoubi A, Roversi K, Roversi K, Lucido CT, Restaino AC, Huang S, *et al*: Nociceptor neurons affect cancer immunosurveillance. Nature 611: 405-412, 2022.
31. Zhang Y, Lin C, Liu Z, Sun Y, Chen M, Guo Y, Liu W, Zhang C, Chen W, Sun J, *et al*: Cancer cells co-opt nociceptive nerves to thrive in nutrient-poor environments and upon nutrient-starvation therapies. Cell Metab 34: 1999-2017.e10, 2022.
32. Qiao N, Dai X, Chen J, Cao H, Hu G, Guo X, Liu P, Xing C and Yang F: Single nucleus RNA sequencing reveals cellular and molecular responses to vanadium exposure in duck kidneys. J Hazard Mater 480: 136492, 2024.
33. Yamada Y, Koshizuka K, Hanazawa T, Kikkawa N, Okato A, Idichi T, Arai T, Sugawara S, Katada K, Okamoto Y and Seki N: Passenger strand of miR-145-3p acts as a tumor-suppressor by targeting MYO1B in head and neck squamous cell carcinoma. Int J Oncol 52: 166-178, 2018.
34. Zhou X, Wang R, Li X, Yu L, Hua D, Sun C, Shi C, Luo W, Rao C, Jiang Z, *et al*: Splicing factor SRSF1 promotes gliomagenesis via oncogenic splice-switching of MYO1B. J Clin Invest 129: 676-693, 2019.
35. Chen YH, Xu NZ, Hong C, Li WQ, Zhang YQ, Yu XY, Huang YL and Zhou JY: Myo1b promotes tumor progression and angiogenesis by inhibiting autophagic degradation of HIF-1α in colorectal cancer. Cell Death Dis 13: 939, 2022.
36. Wang H, Yang F, Ye J, Dai X, Liao H, Xing C, Jiang Z, Peng C, Gao F and Cao H: Ginkgo biloba extract alleviates deltamethrin-induced testicular injury by upregulating SKP2 and inhibiting Beclin1-independent autophagy. Phytomedicine 135: 156245, 2024.
37. Zhang D, Qian C, Wei H and Qian X: Identification of the prognostic value of tumor microenvironment-related genes in esophageal squamous cell carcinoma. Front Mol Biosci 7: 599475, 2020.
38. Shao Y, Li W, Zhang L, Xue B, Chen Y, Zhang Z, Wang D and Wu B: CDH13 is a prognostic biomarker and a potential therapeutic target for patients with clear cell renal cell carcinoma. Am J Cancer Res 12: 4520-4544, 2022.
39. Gao H, Wei H, Yang Y, Li H, Liang J, Ye J, Zhang F, Wang L, Shi H, Wang J and Han A: Phase separation of DDX21 promotes colorectal cancer metastasis via MCM5-dependent EMT pathway. Oncogene 42: 1704-1715, 2023.
40. Wang S, Zhang Y, Cai Q, Ma M, Jin LY, Weng M, Zhou D, Tang Z, Wang JD and Quan Z: Circular RNA FOXP1 promotes tumor progression and Warburg effect in gallbladder cancer by regulating PKLR expression. Mol Cancer 18: 145, 2019.
41. Chen WY, Thuy Dung PV, Yeh HL, Chen WH, Jiang KC, Li HR, Chen ZQ, Hsiao M, Huang J, Wen YC and Liu YN: Targeting PKLR/MYCN/ROMO1 signaling suppresses neuroendocrine differentiation of castration-resistant prostate cancer. Redox Biol 62: 102686, 2023.
42. Peng J, Dai X, Zhang T, Hu G, Cao H, Guo X, Fan H, Chen J, Tang W and Yang F: Copper as the driver of the lncRNA-TCONS-6251/miR-novel-100/TC2N axis: Unraveling ferroptosis in duck kidney. Int J Biol Macromol 282: 136797, 2024.
43. Li H, Wang Z, Liang H, Liu X, Liu H, Zhuang Z and Hou J: Depletion of PHLDB2 suppresses epithelial-mesenchymal transition and enhances anti-tumor immunity in head and neck squamous cell carcinoma. Biomolecules 14: 232, 2024.
44. Chen J, Dai X, Xing C, Zhang Y, Cao H, Hu G, Guo X, Gao X, Liu P and Yang F: Cooperative application of transcriptomics and ceRNA hypothesis: lncRNA-00742/miR-116 targets CD74 to mediate vanadium-induced mitochondrial apoptosis in duck liver. J Hazard Mater 480: 135904, 2024.
45. Chen G, Zhou T, Ma T, Cao T and Yu Z: Oncogenic effect of PHLDB2 is associated with epithelial-mesenchymal transition and E-cadherin regulation in colorectal cancer. Cancer Cell Int 19: 184, 2019.
46. Kang W, Zhang J, Huang T, Zhou Y, Wong CC, Chan RCK, Dong Y, Wu F, Zhang B, Wu WKK, *et al*: NOTCH3, a crucial target of miR-491-5p/miR-875-5p, promotes gastric carcinogenesis by upregulating PHLDB2 expression and activating Akt pathway. Oncogene 40: 1578-1594, 2021.